AIAA JOURNAL
Vol. 48, No. 11, November 2010

Technical Notes

Modification of Ninth-Order Weighted Essentially Nonoscillatory Scheme for Mixed Subsonic/Supersonic Flow

A. Gross* and H. F. Fasel†
University of Arizona, Tucson, Arizona 85721

DOI: 10.2514/1.J050361

I. Introduction

THIS Note describes a modification to the high-order-accurate weighted essentially nonoscillatory (WENO) scheme implementation by Gross and Fasel [1,2]. The motivation behind this effort was to have a high-order-accurate discretization for the convective fluxes that works equally well for subsonic and supersonic flows. The schemes described in this Note are based on schemes by Jiang and Wu [3] and Balsara and Shu [4].

In [2], we discussed a procedure for constructing high-order-accurate upwind schemes. We suggested reconstructing the flow variables at the left (L) and right side (R) of the $i+\frac{1}{2}$ interface using high-order-accurate WENO approximations [3,4] and to employ the Roe scheme [5],

$$F_{i+1/2} = \frac{F^R_{i+1/2} + F^L_{i+1/2}}{2} - |\mathbf{A}|\frac{Q^R_{i+1/2} - Q^L_{i+1/2}}{2} \tag{1}$$

for computing the flux at the cell face. Here, $\mathbf{A} = \partial F/\partial Q = \mathbf{R}\boldsymbol{\Lambda}\mathbf{R}^{-1}$ is the Jacobian of the flux vector F with respect to the state vector Q, and $|\mathbf{A}| = \mathbf{R}|\boldsymbol{\Lambda}|\mathbf{R}^{-1}$. $\mathbf{R}$ is the matrix of right eigenvectors, and $\boldsymbol{\Lambda}$ is the eigenvalue matrix of $\mathbf{A}$. Matrix $|\mathbf{A}|$ is computed from the Roe average of Q^R and Q^L and the $i+1/2$ interface metrics. When the ninth-order-accurate [$\mathcal{O}(9)$] WENO approximation is employed, the left and right states are obtained from

$$\begin{aligned} Q^L_{i+1/2} = {} & \tfrac{1}{840}(-3Q_{i-3} + 29Q_{i-2} - 139Q_{i-1} + 533Q_i \\ & + 533Q_{i+1} - 139Q_{i+2} + 29Q_{i+3} - 3Q_{i+4}) \\ & - \mathbf{R}_{i+1/2}\varphi_N(\Delta\hat{Q}_{i-7/2}, \Delta\hat{Q}_{i-5/2}, \Delta\hat{Q}_{i-3/2}, \Delta\hat{Q}_{i-1/2}, \\ & \Delta\hat{Q}_{i+1/2}, \Delta\hat{Q}_{i+3/2}, \Delta\hat{Q}_{i+5/2}, \Delta\hat{Q}_{i+7/2}) \end{aligned} \tag{2}$$

$$\begin{aligned} Q^R_{i+1/2} = {} & \tfrac{1}{840}(-3Q_{i-3} + 29Q_{i-2} - 139Q_{i-1} + 533Q_i \\ & + 533Q_{i+1} - 139Q_{i+2} + 29Q_{i+3} - 3Q_{i+4}) \\ & + \mathbf{R}_{i+1/2}\varphi_N(\Delta\hat{Q}_{i+9/2}, \Delta\hat{Q}_{i+7/2}, \Delta\hat{Q}_{i+5/2}, \Delta\hat{Q}_{i+3/2}, \\ & \Delta\hat{Q}_{i+1/2}, \Delta\hat{Q}_{i-1/2}, \Delta\hat{Q}_{i-3/2}, \Delta\hat{Q}_{i-5/2}) \end{aligned} \tag{3}$$

which are a central interpolation combined with a WENO part φ_N that employs smoothness estimators for placing less weight on stencils that are computed from discontinuous parts of the solution. The differences of the characteristic variables are computed as $\Delta\hat{Q}_{k+1/2} = \hat{Q}_{k+1} - \hat{Q}_k$ with $\hat{Q}_k = \mathbf{R}^{-1}_{i+1/2}Q_k$. The matrices $\mathbf{R}_{i+1/2}$ and $\mathbf{R}^{-1}_{i+1/2}$ are computed from quantities at the cell face $i+1/2$, which are computed by Roe-averaging quantities from i and $i+1$. This widely used approach affects the order of the scheme only indirectly, as the matrices employed for the forward and backward transformations are computed from the same averages. Further details and coefficients can be found in [1,2]. In this Note, this $\mathcal{O}(9)$ scheme is referred to as scheme 1 (S1). This scheme was employed extensively and successfully for simulating time-dependent subsonic flows such as Tollmien–Schlichting (T–S) waves in a flat-plate boundary layer and laminar separation bubbles on low-pressure turbine blades [2].

We noticed that when we employed the same scheme for computing T–S waves in supersonic boundary layers, the residuals did not drop down to machine accuracy, indicating undesirable residue disturbances in the solution. Therefore, following the approach outlaid in [3], we developed a flux-splitting-based $\mathcal{O}(9)$ WENO scheme. We considered the Lax–Friedrichs (L–F) splitting,

$$\hat{F}^{\pm}_k = \tfrac{1}{2}(\hat{F}_k \pm |\lambda_{\max}|\hat{Q}_k) \tag{4}$$

where $|\lambda_{\max}|$ was taken as the largest $|u| + c$ over the local range (the interval over which the stencils are computed), and $\hat{F}_k = \mathbf{R}^{-1}_{i+1/2}F_k$. The fluxes at k are computed with the $i+1/2$ interface metrics. In this Note, this scheme will be referred to as L–F. We also considered a flux splitting,

$$\hat{F}^{\pm}_k = \tfrac{1}{2}(\hat{F}_k \pm |\boldsymbol{\Lambda}_{i+1/2}|\hat{Q}_k) \tag{5}$$

where the entire eigenvalue matrix $\boldsymbol{\Lambda}_{i+1/2}$ was considered and evaluated locally. The purpose of this Note is to demonstrate that this scheme works better for mixed subsonic/supersonic flows. In our simulations, we found the WENO scheme to perform better for subsonic flows when it was based on the Roe scheme [Eq. (1)] with full matrix $|\mathbf{A}|$ instead of the spectral radius assumption, $|\mathbf{A}| \approx |\lambda_{\max}|\mathbf{I}$, and it was found to perform better for supersonic flows when it was based on the L–F splitting [Eq. (4)]. The idea was that, by blending elements from both approaches, a scheme could be obtained that was suitable for mixed subsonic/supersonic flows. The numerical flux is now computed as

$$\begin{aligned} F_{i+1/2} = {} & \tfrac{1}{840}(-3F_{i-3} + 29F_{i-2} - 139F_{i-1} + 533F_i \\ & + 533F_{i+1} - 139F_{i+2} + 29F_{i+3} - 3F_{i+4}) \\ & + \mathbf{R}_{i+1/2}[-\varphi_N(\Delta\hat{F}^+_{i-7/2}, \Delta\hat{F}^+_{i-5/2}, \Delta\hat{F}^+_{i-3/2}, \Delta\hat{F}^+_{i-1/2}, \\ & \Delta\hat{F}^+_{i+1/2}, \Delta\hat{F}^+_{i+3/2}, \Delta\hat{F}^+_{i+5/2}, \Delta\hat{F}^+_{i+7/2}) \\ & + \varphi_N(\Delta\hat{F}^-_{i+9/2}, \Delta\hat{F}^-_{i+7/2}, \Delta\hat{F}^-_{i+5/2}, \Delta\hat{F}^-_{i+3/2}, \Delta\hat{F}^-_{i+1/2}, \\ & \Delta\hat{F}^-_{i-1/2}, \Delta\hat{F}^-_{i-3/2}, \Delta\hat{F}^-_{i-5/2})] \end{aligned} \tag{6}$$

where $\Delta\hat{F}^{\pm}_{k+1/2} = \hat{F}^{\pm}_{k+1} - \hat{F}^{\pm}_k$. For this flux-based WENO scheme, we computed the smoothness estimators individually for all flux differences [scheme 2 (S2)] and for the density only [scheme 3 (S3)]. The latter approach was suggested by Balakumar et al. [6].

All results shown in this Note were computed with the aforementioned $\mathcal{O}(9)$ schemes. The viscous fluxes were computed using a shifted control volume approach with fourth-order accuracy, and the solution was integrated in time with a second-order-accurate implicit Adams–Moulton scheme [2]. Instead of one-sided difference stencils and truncated WENO schemes, the ghost cell approach was applied at all boundaries. The resulting adiabatic wall boundary condition

Received 25 November 2009; revision received 11 August 2010; accepted for publication 19 August 2010.

*Assistant Research Professor. Member AIAA.
†Professor. Member AIAA.

does not directly enforce the no-slip condition and is only first-order accurate. Therefore, considerable grid refinement was employed near walls. For supersonic flow, all quantities were specified at the inflow boundary and extrapolated at the freestream and outflow boundaries. For subsonic flow, a characteristics-based boundary condition [7] was employed at all nonwall boundaries.

II. Results

A. Circular Cylinder in Supersonic Flow

We first investigated how the different schemes handled a strong detached shock wave by computing a circular cylinder in supersonic flow. The Reynolds number based on diameter was $Re_D = 1000$, the freestream Mach number was $M = 3$, the freestream temperature was $T_\infty = 300$ K, and the Prandtl number was $Pr = 0.72$. The computational grid had 50×50 cells (indicated in Fig. 1). All cases were computed with a time step of $\Delta t = 10^{-2}$. Isocontours of u velocity are shown in Fig. 1. For schemes 1–3 (S1, S2, and S3), the shock is resolved with 1–2 cells. With L–F splitting, the shock is resolved with 2–3 cells, indicating more numerical diffusion. In Fig. 2, the L_2 norm of the total energy residual is plotted as a function of the time step. A continuous reduction of the residual over time is only obtained with schemes 2 and 3 and L–F splitting. We conclude that the numerical diffusion provided by the L–F splitting is required for stabilizing the solution near the detached shock wave.

B. Tollmien–Schlichting Wave

1. Subsonic Flow

The amplification of T–S waves in a laminar boundary layer is crucially dependent on the accuracy of the wall boundary condition and the discretization. For the following test case, the conditions documented in section 5.3 of Wasistho et al. [8] were chosen. The computational grid and case were the same as in [2]. The Mach number was 0.5; the unit Reynolds number was 100,000; the inflow Reynolds number was 100,000; and the freestream temperature was 300 K. The dimensions of the computational domain were 8.64×2.5 with 770×196 cells in the downstream and wall normal directions. The near-wall grid line spacing was 0.000231. Disturbances with a frequency of 1.2732 were introduced by wall normal blowing and suction, with an amplitude of 10^{-5}, through a forcing slot located between 0.11221 to 0.38151. A compressible boundary-layer similarity solution was prescribed as the initial condition. The time step was 0.007854.

The time history of the L_2 norm of the residual of the total energy ρe for the base flow calculations (boundary layer without disturbances) is shown in Fig. 3. With scheme 3 and L–F splitting, the base flow could not be computed. For schemes 1 and 2, the residual was converged down to machine accuracy. After convergence of the base flow, a T–S wave was introduced through the disturbance slot. An instantaneous visualization of the v-velocity disturbance for scheme 1 is shown in Fig. 4. An identical visualization was obtained for scheme 2. The wave amplitude is seen to grow and decay in the downstream direction. To more quantitatively assess the result, the time-dependent data were Fourier transformed in time, and the disturbance amplitudes were extracted (Fig. 5). Since our new results provide a good match with earlier reference data by Wasistho et al. [8], we concluded that both schemes were appropriate for computing T–S waves in subsonic flows.

2. Supersonic Flow

We also computed a T–S wave in a supersonic boundary layer with an adiabatic wall. The Mach number was $M = 1.6$; the unit Reynolds number was 100,000; the domain length and height were 10×5; and the inflow Reynolds number was 26,430. The Prandtl number was 0.72, and the freestream temperature was 300 K. For $0.4 < x < 1.05$,

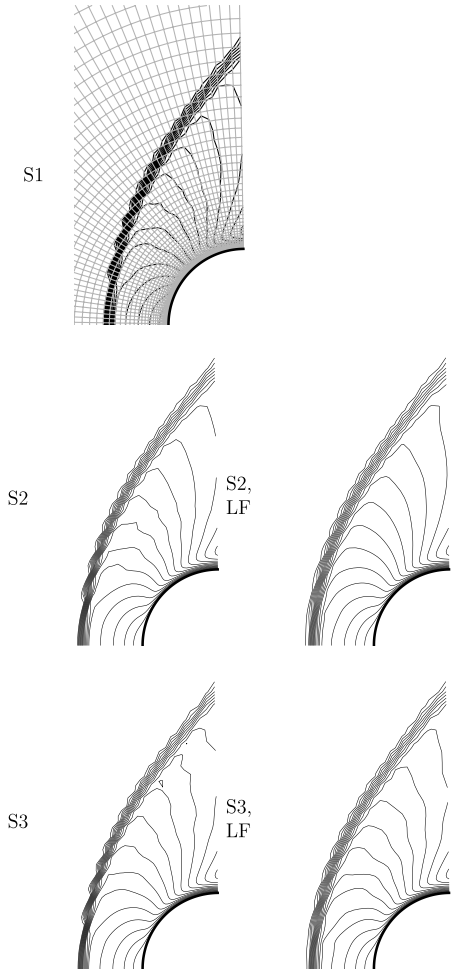

Fig. 1 Cylinder at $M = 3$ and $Re_D = 1000$. Computational grid near cylinder and isocontours of u velocity (increment 0.1).

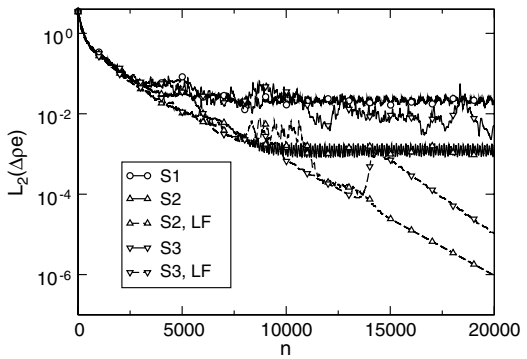

Fig. 2 Cylinder at $M = 3$ and $Re_D = 1000$. L_2 norm of total energy residual.

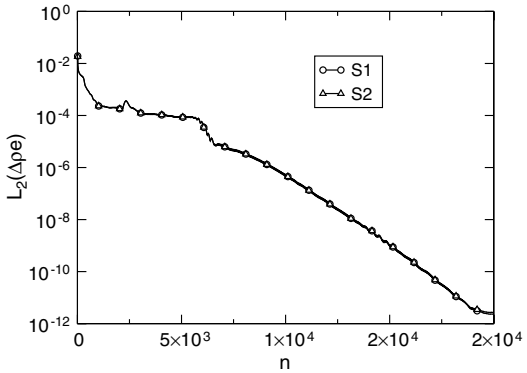

Fig. 3 Base flow calculations for $M = 0.5$ and $Re = 100,000$. L_2 norm of total energy residual.

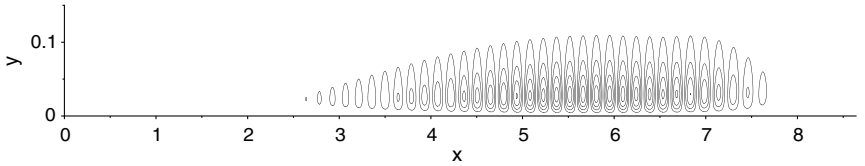

Fig. 4 T–S wave for $M = 0.5$ and $Re = 100,000$. Isocontours of v-disturbance amplitude (increment 5×10^{-5}).

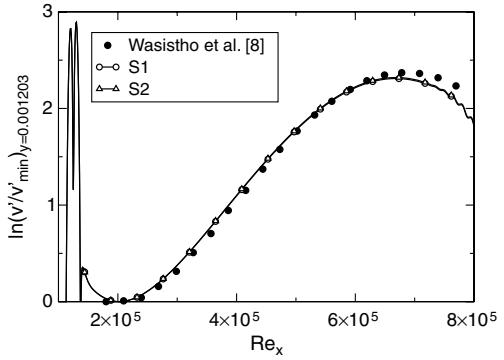

Fig. 5 T–S wave for $M = 0.5$ and $Re = 100,000$. v-disturbance amplitude at $y = 0.001203$.

disturbances with a frequency of 0.795775 were introduced through wall normal blowing and suction with an amplitude of 10^{-5}. These conditions are approximately the same as those for case A1 in [9]. The computational grid had 200×300 cells and a minimum near-wall grid line spacing of 0.0004. The computational time step was 0.02512. The convergence histories for the base flow are compared in Fig. 6. Full convergence of the base flow is accomplished only with scheme 2. Instantaneous visualizations of the ρv-disturbance amplitude are shown in Fig. 7. For scheme 1, disturbances that appear to be originating from the inflow boundary contaminate the solution. These undesirable disturbances motivated the modification of the scheme reported upon in this Note. With scheme 2, a clean disturbance field is obtained, while with scheme 3 (smoothness estimation based on density only), the disturbance flow could only be computed with L–F splitting. Then, however, the flowfield was found to be

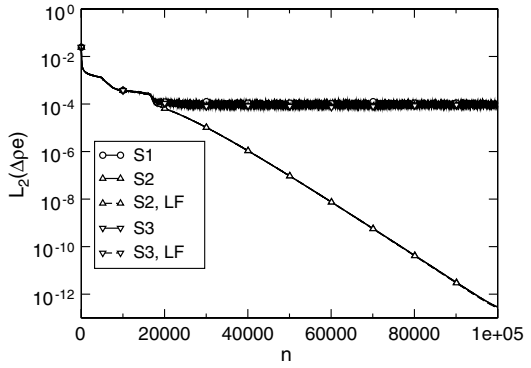

Fig. 6 Base flow calculations for $M = 1.6$ and $Re = 100,000$. L_2 norm of total energy residual.

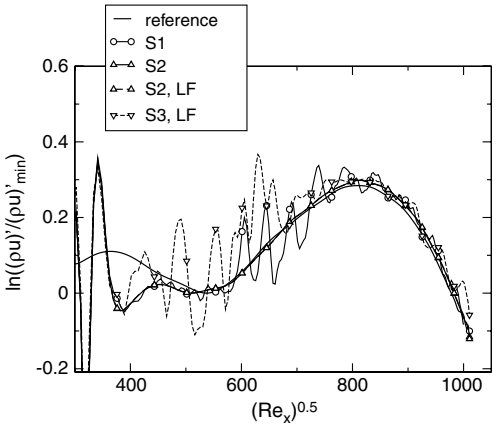

Fig. 8 T–S wave for $M = 1.6$ and $Re = 100,000$. Wall normal maximum of ρu-disturbance amplitude.

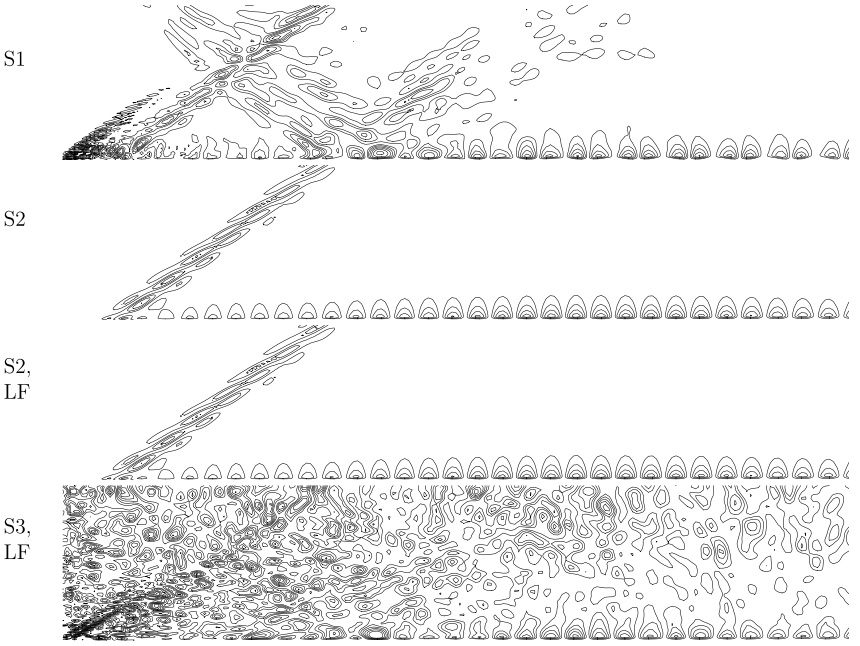

Fig. 7 T–S wave for $M = 1.6$ and $Re = 100,000$. Isocontours of a ρv disturbance (increment 5×10^{-6}).

Table 1 Computed order of accuracy and computational effort

Scheme	Order of accuracy	Wall clock time, s
S1	8.50	640
S2	8.50	855
S2, L–F	8.13	714
S3	8.49	593
S3, L–F	8.07	480

strongly contaminated with numerical noise. A comparison of the computed ρu-disturbance amplitudes is shown in Fig. 8.[‡] Figure 8 illustrates that the wave amplitude distribution is captured only approximately with schemes 1 and 3. A smooth disturbance amplitude distribution is obtained only with scheme 2. Since a comparably good result for a T–S wave in a subsonic boundary layer was also obtained with scheme 2, we conclude that this scheme is appropriate for simulations with mixed subsonic and supersonic flow. Appropriate measures will have to be taken to stabilize the scheme near strong shock waves.

C. Accuracy and Computational Effort

We also computed the accuracy of the various schemes for the smooth grid inviscid vortex convection problem described in [2]. The problem consists of a vortex that is convected over a given downstream distance. Because the viscous dissipation is zero, the vortex should maintain its shape. An error can be defined by considering the root mean square of the difference in the u-velocity distributions of the computed convected vortex and the analytical function that was employed for generating the vortex [2]. From the error obtained on two different grids (387×129 and 195×65), we computed the order of accuracy. Results and wall clock times (for the finer grid) are provided in Table 1 (all cases were computed on 64 processors, on an IBM P5+). The computed order of accuracy is slightly lower than the formal accuracy but consistent with earlier results [2]. With L–F splitting, the computational effort is reduced by about 20%. The computed order of accuracy is, however, lower. When the smoothness estimation is based on the density, the computational effort is reduced by about 30%. Scheme 2 is about 30% more computer time intensive than scheme 1. This can be explained by the higher operations count resulting from the additional transformation $\hat{F}_k = \mathbf{R}_{i+1/2}^{-1} F_k$.

III. Conclusions

A ninth-order-accurate WENO scheme was modified for enhanced computations of mixed subsonic and supersonic flows. Examples demonstrate deficiencies of the original method and benefits of the improvements. In particular, it is shown that with the modified scheme, residuals of mixed subsonic/supersonic flows can be converged down to machine accuracy. This is especially crucial for stability simulations where the disturbance amplitudes are typically many orders of magnitude smaller than the corresponding reference quantities. The modification of the scheme results in an approximately 30% higher computational cost.

Acknowledgments

This work was funded by the U. S. Air Force Office of Scientific Research, under grant number F9550-08-1-0211, with John Schmisseur serving as Program Manager. The authors are indebted to A. Laible for providing the reference data for the T–S wave in a supersonic boundary layer.

References

[1] Gross, A., and Fasel, H. F., "High-Order WENO Schemes Based on the Roe Approximate Riemann Solver," AIAA Paper 2002-2735, June 2002.

[2] Gross, A., and Fasel, H. F., "High-Order Accurate Numerical Method for Complex Flows," *AIAA Journal*, Vol. 46, No. 1, 2008, pp. 204–214. doi:10.2514/1.22742

[3] Jiang, G. S., and Wu, C. C., "A High-Order WENO Finite Difference Scheme for the Equations of Ideal Magnetohydrodynamics," *Journal of Computational Physics*, Vol. 150, No. 2, 1999, pp. 561–594. doi:10.1006/jcph.1999.6207

[4] Balsara, D. S., and Shu, C. W., "Monotonicity Preserving Essentially Non-Oscillatory Schemes with Increasingly High Order of Accuracy," *Journal of Computational Physics*, Vol. 160, No. 2, 2000, pp. 405–452. doi:10.1006/jcph.2000.6443

[5] Roe, P. L., "Approximate Riemann Solvers, Parameter Vectors and Difference Schemes," *Journal of Computational Physics*, Vol. 43, No. 2, 1981, pp. 357–372. doi:10.1016/0021-9991(81)90128-5

[6] Balakumar, P., Zhao, H., and Atkins, H., "Stability of Hypersonic Boundary-Layers over a Compression Corner," AIAA Paper 2002-2848, June 2002.

[7] Gross, A., and Fasel, H. F., "Characteristic Ghost-Cell Boundary Condition," *AIAA Journal*, Vol. 45, No. 1, 2007, pp. 302–306. doi:10.2514/1.23130

[8] Wasistho, B., Geurts, B. J., and Kuerten, J. G. M., "Simulation Techniques for Spatially Evolving Instabilities in Compressible Flow over a Flat Plate," *Computers and Fluids*, Vol. 26, No. 7, 1997, pp. 713–739. doi:10.1016/S0045-7930(97)00021-2

[9] Thumm, A., "Numerische Untersuchungnen zum Laminar-Turbulenten Strömungsumschlag in Transsonischen Grenzschichtströmungen," Ph.D. Dissertation Univ. Stuttgart, Germany, 1991.

X. Zhong
Associate Editor

[‡]The reference data were provided by A. Laible, University of Arizona, Department of Aerospace and Mechanical Engineering, Tucson, AZ (private communication), and obtained with a high-order-accurate finite difference code on a grid with sufficient resolution.